Electron dose dependence of signal-to-noise ratio, atom contrast and resolution in transmission electron microscope images

Z. Lee *, H. Rose, O. Lehtinen, J. Biskupek, U. Kaiser

Universität Ulm, Materialwissenschaftliche Elektronenmikroskopie, Albert-Einstein-Allee 11, 89081 Ulm, Germany

ARTICLE INFO

ABSTRACT

In order to achieve the highest resolution in aberration-corrected (AC) high-resolution transmission electron microscopy (HRTEM) images, high electron doses are required which only a few samples can withstand. In this paper we perform dose-dependent AC-HRTEM image calculations, and study the dependence of the signal-to-noise ratio, atom contrast and resolution on electron dose and sampling. We introduce dose-dependent contrast, which can be used to evaluate the visibility of objects under different dose conditions. Based on our calculations, we determine optimum samplings for high and low electron dose imaging conditions.

© 2014 Elsevier B.V. All rights reserved.

1. Introduction

The instrumental resolution of transmission electron microscopes (TEMs) has dramatically improved during the last decade, mainly due to the introduction and practical realisation of hardware aberration correction [1–3]. As a result, materials can now be imaged and identified down to single atomic columns [4,5] or, in the case of the new class of two-dimensional materials, even single atoms [6,7]. With the aim of reducing radiation damage induced by the imaging electrons, low-voltage aberration-corrected TEMs, down to voltages of 20 kV [8,9], 30 kV [10], and 40 kV [11], are currently under development. A voltage-tunable fully-corrected (that is, corrected for higher-order geometrical aberrations as well as chromatic aberrations of the imaging lenses [12]) TEM seems close to becoming reality [13].

Achieving the improved resolution of an aberration-corrected TEM requires, however, an infinite electron dose on the studied specimen, and only few materials can withstand very high, let alone infinite doses. Materials can be damaged via the knock-on damage mechanism, where atoms are displaced by direct impacts of the imaging electrons, and in such cases lowering of the electron energy below a material specific threshold is desirable [8,14–17]. On the other hand, the electron–electron (inelastic) scattering cross section increases at lower electron energies and, depending on the material, ionization can become the dominating damage mechanism [17]. Effective ways of reducing ionization damage may be cooling of the specimen [18] or conductive coating [19]. As extreme examples of the latter, samples have been enclosed within carbon nanotubes [9], or between graphene layers [20], greatly reducing radiation damage during imaging. Such approaches are not always feasible, however, and images thus need to be acquired with limited electron doses.

The stability of the microscope is another factor limiting the electron dose in a single image. The microscope tends to drift away from the corrected state, and as a result images can be acquired only within a small time window before resolution is deteriorated [21–23]. Also all kinds of instabilities including electrostatic and magnetic field noise [24] and instabilities caused by the sample stage can lead to blurring of the images, if long exposure times are used.

With all this in mind, microscopists have to develop strategies for limited electron dose imaging. Thus, having a robust framework for estimating the effects of this limitation is necessary. Here, we address this issue, by exploring the influence of the electron dose and sampling on the signal-to-noise ratio (SNR), the atom or lattice contrast, as well as the resolution, with the help of dose-dependent image simulations. We introduce a modified definition for the image contrast, which takes the electron dose into account. The dose related noise is treated as stochastic fluctuations around the ideal electron count at each image pixel, instead of the previously used additive noise [25–30]. Using these tools, we determine the optimal sampling for achieving atomic resolution images of graphene, as a function of the information limit and magnification of the microscope, as well as determine the required electron dose based on the calculated atom contrast. Graphene is used as the example material due to the simplicity of its structure, which allows straight forward interpretation of the results.

* Corresponding author.
  E-mail address: zhongbo.lee@uni-ulm.de (Z. Lee).

2. Theoretical and experimental methods

2.1. Image simulation with finite electron dose

The structural information of the sample is carried primarily by elastically scattered electrons, which is distorted by an electromagnetic lens during the propagation process in the microscope. The distorted information is transferred to the detector and the average number of electrons collected by each detector pixel is determined by the electron dose, the sampling and the probability of the electron to be found on each pixel, which is the squared modulus of the image wave. The actual number of electrons collected by each detector pixel is governed by Poisson statistics.

In this paper we utilize the elastic model based on [31] in the image calculation for graphene at low voltages ranging from 20 kV to 80 kV on a C_s/C_c−corrected microscope. Inelastic scattering is not included for the following reason:

On a C_c−corrected microscope, the contrast delocalization caused by inelastic scattering in a single layer of graphene at voltages as low as 20 kV is negligible. In this case, the influence of inelastic scattering on the image is mainly the decrease of the intensity contributed by the elastic scattered electrons [32].Our image simulation with finite electron dose follows the order:

1. Generate the position distribution function. Obtain the probability distribution of the electrons by calculating the image intensity for the experimental imaging conditions with infinite dose. The experimental conditions include the accelerating voltage, aberration parameters, the size of the usable aperture determined by the aberration corrector and the damping functions. Since we search for the image conditions providing the maximum contrast, we determine the parameters giving the brightest atom contrast. The general procedure to search for the maximum contrast and the corresponding imaging conditions are presented in [31]. In addition, we include the influence of image spread E_{is}, focus spread E_{fs} and the MTF of the camera. For a phase object, the intensity I_i of the final image is a convolution between the calculated image I [31] and the damping functions:

$$I_i(\vec{\rho}) = \int \tilde{I}(\vec{q})E_{is}(\vec{q})E_{fs}(\vec{q})MTF(\vec{q})e^{i\vec{q}\cdot\vec{\rho}}\, d^2\vec{q}. \tag{1}$$

Image spread is caused by all kinds of noise causing a random deflection of the image. The origin of these zeroth-order aberrations is vibrations and drift of the stage, parasitic time-dependent fields resulting from instabilities of the lens currents and magnetic fields resulting from eddy currents in the material of the lenses as shown recently by Uhlemann et al. [24]. The combined effect of these disturbances on the image contrast is given by the envelope function [12]

$$E_{is}(\vec{q}) = \exp[-\tfrac{1}{2}(2\pi\sigma(C_\epsilon))^2 q^2]. \tag{2}$$

The spatial frequency $q = \theta/\lambda$ depends on the scattering angle θ and the wavelength λ of the electrons; $\sigma(C_\epsilon)$ denotes the standard deviation of the image spread.

The residual focus spread is caused by the movement of the stage and all the electromagnetic lenses in the z-direction and by the parasitic first-order aberrations of the focusing elements. The effect of the focus spread on the image contrast is expressed by the envelope function [12]

$$E_{fs}(\vec{q}) = \exp[-\tfrac{1}{2}(\pi\lambda\sigma(C_1))^2 q^4]. \tag{3}$$

Here $\sigma(C_1)$ denotes the standard deviation of the focus spread. In most cases, TEM images are recorded using charge-coupled detectors (CCD) with a fiber-optics coupled scintillator. In the ideal case, each electron is only detected by one of the detector pixels. The number of detected electrons varies from pixel to pixel, resulting in different gray levels. In practice, a single imaging electron can cause signals in more than one pixel because of multiple scattering within the scintillator material and the creation of an excitation volume. This effect is described by the point-spread function (PSF) of the detector, and its Fourier transform is the modulation-transfer function (MTF) [33–35].

The average number of electrons N_j collected by the jth detector pixel is

$$N_j = D\delta^2 I_j, \tag{4}$$

where D represents the electron dose, δ denotes the sampling (pixel size) and I_j is the probability of the electron hitting the jth pixel.

2. The actual number of electrons collected by each detector pixel is generated with random Poisson distribution, indicating that the standard deviation of the number of electrons collected by the jth detector pixel is $\sqrt{N_j}$.

The SNR of the whole image is evaluated as [36]

$$\overline{SNR} = \frac{\overline{N}}{\sigma(N)}, \tag{5}$$

where the average number of electrons per image pixel $\overline{N}$ is defined as

$$\overline{N} = \frac{1}{J}\sum_{j=1}^{J} N_j = \frac{D\delta^2}{J}\sum_{j=1}^{J} I_j = D\delta^2\overline{I}. \tag{6}$$
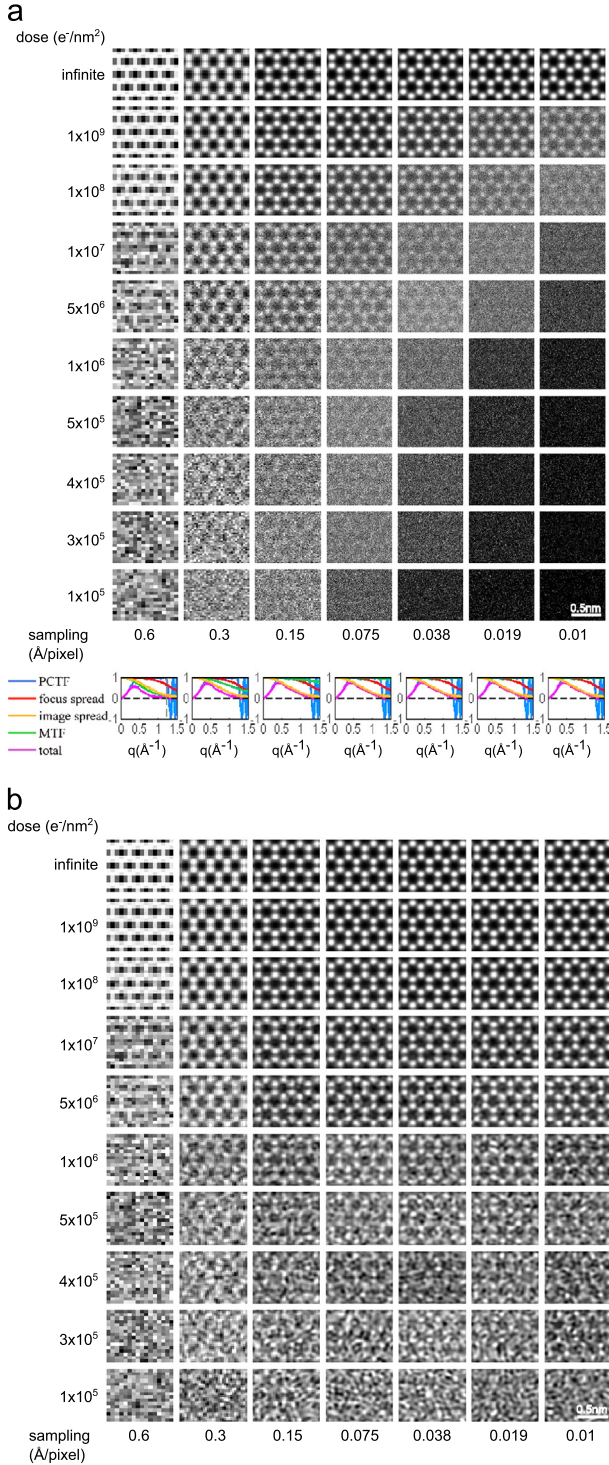
Here J is the total number of pixels and $\overline{I}$ is the average image intensity. $\sigma(N)$ is the standard deviation of the number of electrons collected by each pixel. We define the actual number of electrons collected by the jth image pixel as $Pois(D\delta^2 I_j)$, then

$$\sigma(N) = \sqrt{\frac{1}{J}\sum_{j=1}^{J} [Pois(D\delta^2 I_j) - \overline{Pois(D\delta^2 I_j)}]^2}. \tag{7}$$

If $I_j = \overline{I}$ for any image pixel, indicating the probability of the electrons hitting each image pixel is the same, then $\sigma(N) = \sqrt{D\overline{I}}\delta = \sqrt{\overline{N}}$ and $\overline{SNR} = \sqrt{\overline{N}}$.

2.2. Experimental setup for TEM imaging

Our modeling is based on the characteristics of the prototype SALVE II microscope. This system is based on a Zeiss Libra 200 MC equipped with a Schottky field emitter, an electrostatic Ω-type monochromator and an Ω-type in-column energy-filter. The TEM-platform has been optimized to achieve the highest objective lens current stability ($\Delta I/I < 10^{-7}$) within the voltage range between 20 and 80 kV [8]. The monochromator was used with the largest slit of 60 μm (basically no effect of monochromation) as C_c correction was applied. The size of the energy window of the filter was not limited by an energy-selecting slit but only by the physical limitations such as fixed apertures and tube diameters (about 130 eV at 40 kV). The SALVE II prototype is equipped with an aberration corrector to achieve atomic resolution even at low voltages of 20 and 40 kV, based on the design proposed by Rose [37]. Geometric axial aberrations are corrected up to the 5th order except for C_5, which was designed to be around 4 mm to obtain an optimized phase contrast transfer function. Off-axial aberrations are corrected up to the 3rd order for larger fields of view. The CMOS (complementary metal oxide semiconductor) based camera is the type TVIPS T416 (4k detector, 16×16 μm^2 pixel size). The fiber-optics coupled scintillator was optimized to obtain large conversion rates for high sensitivity and very small thickness for high resolution.

Table 1
Aberration parameters and image spread used for the simulation of images at an accelerating voltage of 20 kV, 40 kV, 60 kV and 80 kV on the C_s/C_c-corrected SALVE II microscope. The usable aperture determined by the maximum size of the usable phase plate is 50 mrad. C_s is the coefficient of the third-order spherical aberration; Δf is the defocus and $\sigma(C_c)$ represents the standard deviation of image spread.

HT (kV)	$C_s(\mu m)$	$\Delta f(\text{Å})$	$\sigma(C_c)$ (pm)
20	− 13	98	47
40	− 12	80	40
60	− 11.5	72	29
80	− 11.5	70	26

3. Results

In order to study the dependence of SNR, atom contrast and specimen resolution on electron dose and sampling, we have simulated images of graphene obtained with the C_c/C_s-corrected SALVE II microscope operated at an accelerating voltage of 80 kV (Fig. 1). Subsequently, we have determined the optimum sampling based on the previous study for 20 kV, 40 kV, 60 kV and 80 kV.

The MTF data (Fig. A1) for the SALVE microscope at 20 kV, 40 kV, 60 kV and 80 kV were previously measured using averaged single electron events detected by the T416 camera [38,39].

Parameters used for the image simulations of the SALVE II microscope are listed in Table 1. The defocus Δf and the coefficient C_s of the third-order spherical aberration are free parameters; $C_5 = 4$ mm, $C_c = 0$ and residual focus spread $\sigma(C_1) = 5$ Å are fixed for all accelerating voltages.

In the following subsections we are evaluating step by step the dependence of SNR (Section 3.1), atom contrast (Section 3.2) and specimen resolution (Section 3.3) on dose and sampling. Based on these studies, we will determine the optimum sampling for imaging condition with finite dose in Section 3.4.
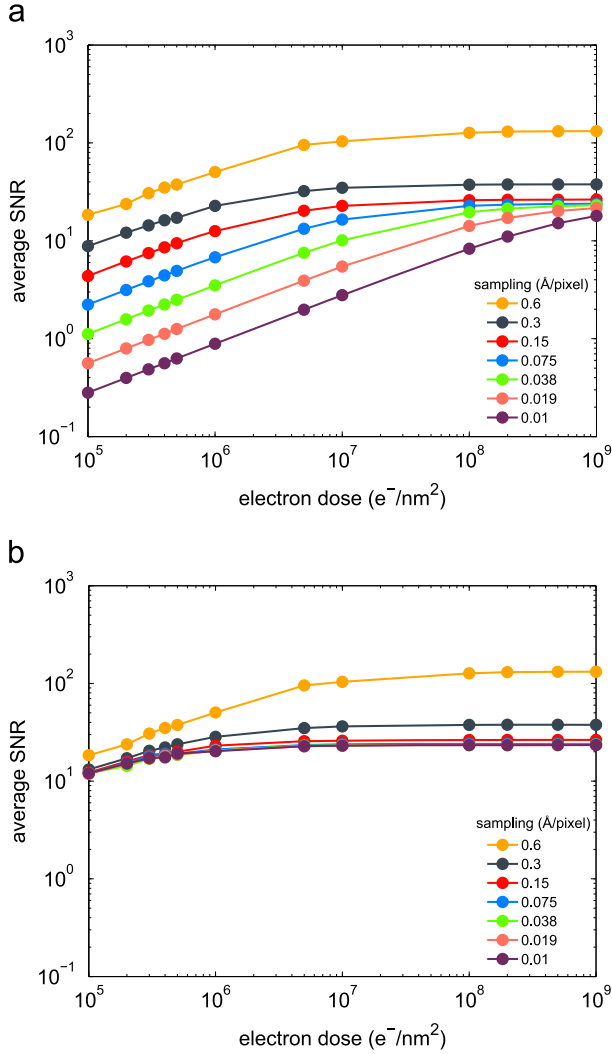
3.1. Dependence of SNR on dose and sampling

Each row and each column in Fig. 1a show the evolution of the object visibility with respect to the sampling and dose, respectively. As the sampling gets finer from left to right, the object visibility ameliorates first, then declines. The object visibility increases with the dose (Fig. 1 every column from bottom to top). The influence of the camera MTF can be ignored for sampling finer than 0.15 Å/pixel (green lines in CTF plot), since in these cases the MTF is always 1 within the range of spatial frequency marked. The damping of the image spread (yellow line) is much stronger than the focus spread (red line) at 80 kV for the SALVE II microscope.

Fig. 2a shows that the SNRs of the images calculated for different samplings (Fig. 1a) increase with the dose linearly at a logarithmic scale for doses smaller than 5×10^6 e$^-$/nm^2, and converge gradually towards the maximum SNRs obtained for infinite dose. The maximum SNR increases with the sampling. The behavior in Fig. 2a can be actually understood by discussing Eqs. (5) and (7). In the low-dose cases, since the number of electrons on each image pixel $D\delta^2 I_j$ is close to the average $D\delta^2\bar{I}$, we can replace $Pois(D\delta^2 I_j)$ with $Pois(D\delta^2\bar{I})$ and obtain

$$\sigma(N) = \sqrt{\frac{1}{J}\sum_{j=1}^{J}[Pois(D\delta^2 I_j) - \overline{Pois(D\delta^2 I_j)}]^2}$$

$$\approx \sqrt{\frac{1}{J}\sum_{j=1}^{J}[Pois(D\delta^2\bar{I}) - \overline{Pois(D\delta^2\bar{I})}]^2} = \sqrt{D\bar{I}}\delta = \sqrt{N}, \quad (8)$$

Fig. 1. (a) Calculated HRTEM images of graphene for different doses and samplings with a usable aperture of 50 mrad under an acceleration voltage of 80 kV. The last row in (a) shows the CTF for different samplings. The PCTF function (blue), focus spread envelope (red) and image spread envelope (yellow) are the same for each column. The MTF (green) depends on the sampling and in order to minimize the damping of MTF on the image contrast for graphene, samplings finer than 0.15 Å/pixel are required. The total contrast transfer function (purple) is a product of all the functions mentioned above. All images are displayed with the maximum contrast, namely the image intensities are mapped on the full grayscale values ranging between 0 and 255. Vertical dashed lines in the plots show the maximum spatial frequency achievable for the sampling written above. (b) Sharp-cutoff low-pass filtered images of (a). The radius of the low-pass filter applied for each image is determined by the information limit, which depends on the PCTF and all damping functions (CTF plots in a). (For interpretation of the references to color in this figure caption, the reader is referred to the web version of this paper.)

a

b

Fig. 2. Average SNR as a function of the electron dose and sampling based on Fig. 1: (a) unfiltered, (b) sharp-cutoff low-pass filtered. The calculation is performed for the accelerating voltage of 80 kV.

$$\overline{SNR} = \frac{\overline{N}}{\sigma(N)} \approx \sqrt{D\overline{I}}\delta = \sqrt{\overline{N}}. \tag{9}$$

Therefore log(D) and log(SNR) show a linear behavior with the slope of 1/2 in the low-dose region. In the high-dose cases, $Pois(D\delta^2 I_j) \approx D\delta^2 I_j$ and we obtain

$$\sigma(N) = \sqrt{\frac{1}{J}\sum_{j=1}^{J}[Pois(D\delta^2 I_j) - \overline{Pois(D\delta^2 I_j)}]^2}$$

$$\approx \sqrt{\frac{1}{J}\sum_{j=1}^{J}[D\delta^2 I_j - D\delta^2\overline{I}]^2} = D\delta^2\sigma(I), \tag{10}$$

$$\overline{SNR} = \frac{\overline{N}}{\sigma(N)} \approx \frac{D\delta^2\overline{I}}{D\delta^2\sigma(I)} = \frac{\overline{I}}{\sigma(I)} = const. \tag{11}$$

Here $\sigma(I)$ is the standard deviation of the image calculated with infinite dose and its average intensity $\overline{I}$ is around 1. It should be emphasized that within this definition the variance of the signal itself contributes to $\sigma(I)$.

Fig. 2b shows that after low-pass filtering, the average SNRs of the images are generally improved. Finer sampling results in more remarkable improvement. For the sampling of 0.15 Å/pixel and 0.01 Å/pixel with the electron dose of 1×10^6 e$^-$/nm^2, the average SNRs increase by factors of 1.8 and 23 after the low-pass

filtering, respectively. However, the SNR is not directly related to the visibility of the images. For coarse sampling such as the 1st column in Fig. 1a, the image visibility is rather poor, but the SNR is above 10, higher than in the other cases.

3.2. Dependence of atom contrast on dose and sampling

Contrast originates from the brightness difference between the object and the background. For the measurement of the experimental atom contrast, the intensities of the peak and the valley: I_a and I_b are determined from line profile drawn through the atoms, and the atom contrast is judged with either the modified Weber formula [31]

$$C_W = \frac{I_b - I_a}{I_b} \tag{12}$$

or the Michelson formula [40]

$$C_M = \frac{I_a - I_b}{I_b + I_a}. \tag{13}$$

In the case of very high electron dose, these formulas are correct because the SNRs of the images are high enough so that the disturbance introduced by the electron noise to the image contrast is negligible. However, in an experimental image recorded with low dose, due to the strong statistical fluctuation of the electron counts in the neighbor pixels, the recognition of the object becomes difficult. This statistical influence is not included in Eq. (12) or (13), and the contrast value calculated based on either Eq. (12) or (13) can result in similar contrast values for both high-dose and low-dose images. Fig. 3 shows an example. Fig. 3a and b are extracted from Fig. 1 for the sampling of 0.038 Å/pixel. The intensity difference between the atoms and the background in Fig. 3a (calculated with the dose of 1×10^6 e$^-$/nm^2) is lower than in Fig. 3b (calculated with infinite dose), and the atom visibility in Fig. 3a is therefore lower than in Fig. 3b; however, the contrast evaluation based on the corresponding line profiles Fig. 3c and Fig. 3d with Eq. (12) or (13) produces similar results for both images, which is counter to our visual cognition.

In order to describe the statistical fluctuation in the experimental images, we introduce the term $\sigma(N)/\left[\overline{N}\sigma(I)\right]$. Here $\sigma(N)$ is the standard deviation of the image calculated with finite electron dose, and $\overline{N}\sigma(I)$ is the standard deviation of the image I calculated with infinite dose ($\overline{I} \approx 1$) scaled with the average number of electrons per pixel $\overline{N}$. Based on the discussion in Section 3.1, $\sigma(N)/\left[\overline{N}\sigma(I)\right]$ is approximately proportional to $1/\left[\sqrt{D\overline{I}}\delta\sigma(I)\right]$ under low-dose imaging conditions, and converges towards 1 for high-dose imaging conditions. The trend can be confirmed by Fig. 4. As a result, the influence of the statistical fluctuation is smaller at high dose than at low dose, and smaller for coarse samplings than for fine samplings, generally.

We evaluate the dose-dependent contrast by making one change to Eq. (12).

Our new dose-dependent contrast is defined as

$$C_d = \frac{I_b - I_a}{\left[\frac{\sigma(N)}{\overline{N}\sigma(I)}\right]^\gamma I_b} = \frac{I_b - I_a}{I_b}\left[\frac{\overline{N}\sigma(I)}{\sigma(N)}\right]^\gamma = C_W[SNR \cdot \sigma(I)]^\gamma. \tag{14}$$

A factor $\left[\sigma(N)/(\overline{N}\sigma(I))\right]^\gamma$ is introduced to the denominator. Here γ is positive factor to be determined, and based on Appendix B one can take $\gamma = 2$ for all samplings. The introduction of this term is based on the relation between $\sigma(N)/\left[\overline{N}\sigma(I)\right]$ and atom contrast (Fig. 1a and Fig. 4). The term $\sigma(N)/\left[\overline{N}\sigma(I)\right]$ decreases with respect to the dose, resulting in increased atom contrast. For images calculated with very high dose, $\sigma(N)/\left[\overline{N}\sigma(I)\right]$ converges to 1 and the atom contrast converges to Eq. (12), which is the contrast calculated with infinite dose. For low dose, the term $\sigma(N)/\left[\overline{N}\sigma(I)\right]$ is approximately proportional to $1/\left[\sqrt{\overline{N}}\sigma(I)\right]$, and C_d approaches to 0 when $\overline{N}$ or the dose D
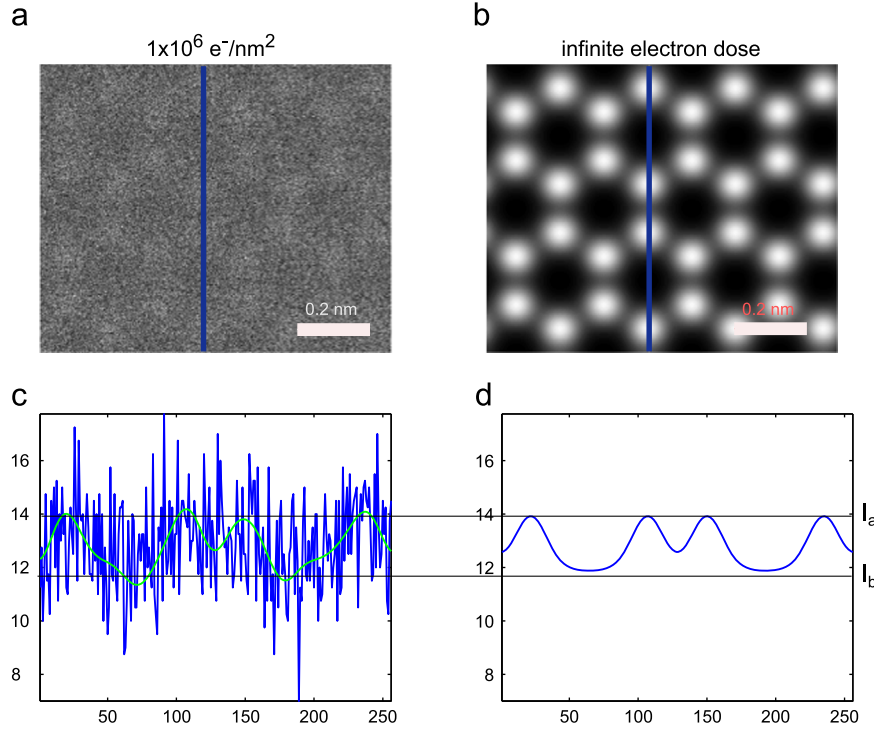
Fig. 3. The atom visibility in the image (a) calculated with the electron dose of 1×10^6 e$^-$/nm^2 is lower than in (b) calculated with infinite dose. However, the conventional methods (Eqs. (12) and (13)) for measuring the atom contrast based on line profiles (c) and (d) produce similar results for the atom contrasts in (a) and (b). Both images are extracted from Fig. 1 for the sampling of 0.038 Å/pixel. The green line in (c) is a smoothed profile of the line profile in (a). (For interpretation of the references to color in this figure caption, the reader is referred to the web version of this paper.)
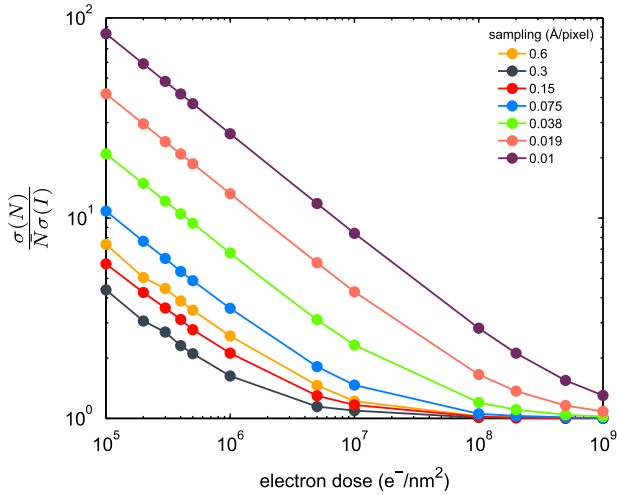
Fig. 4. The term $\log\left[\sigma(N)/(\overline{N}\sigma(I))\right]$ decreases linearly with respect to $\log(D)$ in the low-dose region, and converges towards 1 in the high-dose region. At fixed dose, the value of $\sigma(N)/[\overline{N}\sigma(I)]$ for coarse sampling is generally smaller than for fine sampling. The only exception is the sampling 0.6 Å/pixel, where due to the strong damping of the MTF caused by coarse sampling, $\sigma(I)$ is too small, resulting in $\sigma(N)/[\overline{N}\sigma(I)]$ larger than in the case of 0.3 Å/pixel and 0.15 Å/pixel.

approaches 0. The trend is consistent with what we observe in Fig. 1a.

Fig. 5 shows the atom contrast calculated with Eq. (14) for different samplings and electron doses. The atom contrast increases with respect to the electron dose until it reaches the upper limit. For coarse sampling, the maximum atom contrast as well as the dose required to reach this maximum value is smaller

than for fine sampling. The maximum contrast is 9.4% for the sampling of 0.3 Å/pixel, 14.7% for the sampling of 0.15 Å/pixel, 16.6% for the sampling of 0.075 Å/pixel and 17.2% for the samplings finer than 0.038 Å/pixel. Low-pass filtering (Fig. 5b) can enhance the atom contrast (compared with Fig. 5a) and the effect is especially remarkable for fine samplings.

The distance between two neighbor atoms in graphene is 1.4 Å, and this resolution can be obtained with the lowest dose of 5×10^6 e$^-$/nm^2 at the sampling of 0.15 Å/pixel and 0.075 Å/pixel (Fig. 6a). The dashed line in Fig. 5a shows the maximum atom contrast of 8.6% obtained under this dose condition. Low-pass filtering not only results in atomic resolution at fine samplings ≤ 0.075 Å/pixel (Fig. 6b), but also improves the atom contrast (Fig. 5b). At the sampling of 0.15 Å/pixel under the dose of 5×10^6 e$^-$/nm^2, the contrast is improved to 13%.

3.3. Dependence of specimen resolution on dose and sampling

The attainable specimen resolution d_s is dependent on the electron dose D, SNR and the dose-dependent contrast C_d. We adapt Eq. 3.1 of [15] to include the new dose-dependent contrast and express the specimen resolution as

$$d_s = \sqrt{d_i^2 + \frac{(SNR)^2}{C_d^2 D}}. \tag{15}$$

Here d_i is the instrumental resolution, which is mainly defined by the wavelength λ and the usable aperture UA: $d_i = \lambda/UA$.

Eq. (15) indicates that specimen resolution is a function of the electron dose D and sampling, since SNR and C are functions of the two quantities. The specimen resolution d_s improves as the electron dose increases and reaches the limit of instrumental resolution for infinite dose. Based on the previous calculations on SNR and contrast, we plot the specimen resolution with respect to dose and sampling in
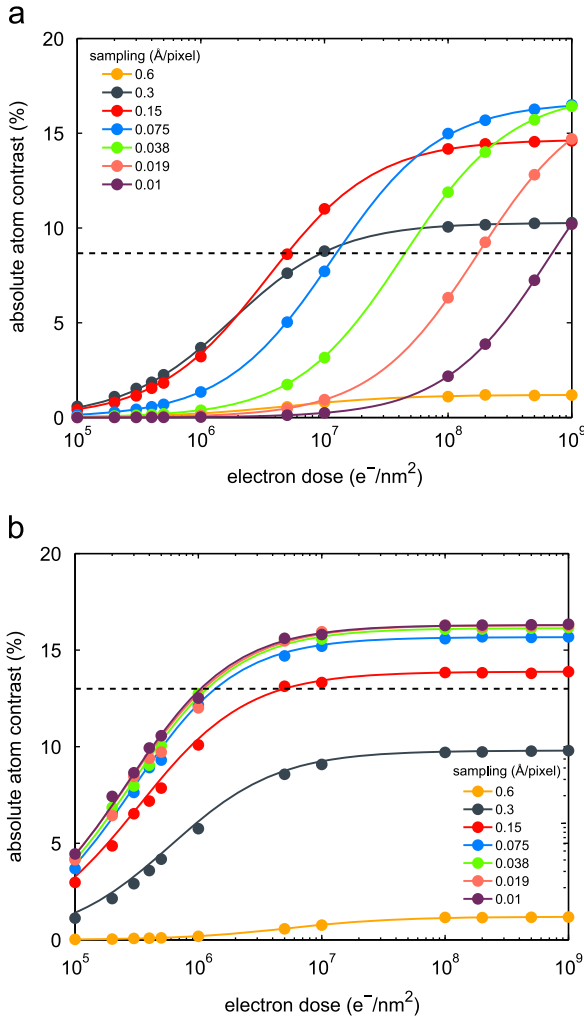
Fig. 5. Atom contrast as a function of the electron dose and sampling. (a) corresponds to Fig. 1(a) and (b) corresponds to Fig. 1b. The atomic resolution of 1.4 Å for graphene is obtained with the lowest dose of $5 \times 10^6 \, e^-/nm^2$ at the sampling of 0.15 Å/pixel and 0.075 Å/pixel (Fig. 6a), and in this case the maximum contrast of 8.6% is obtained under the sampling of 0.15 Å/pixel, marked by the dashed lines. After low-pass filtering, the atom contrast under the same dose is improved to 13%. All calculations are performed for the accelerating voltage of 80 kV.
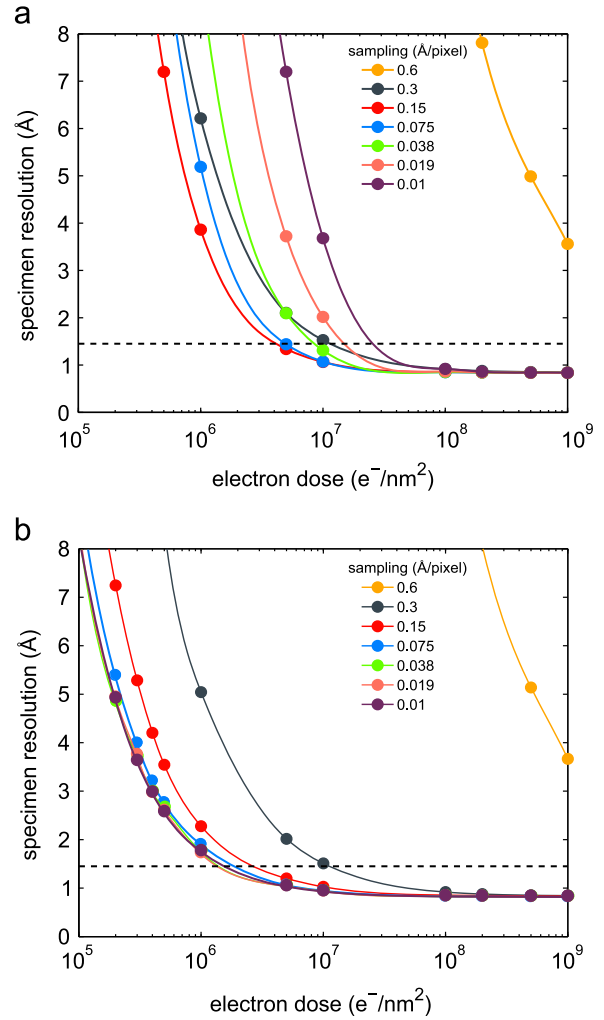
Fig. 6. Specimen resolution as a function of electron dose and sampling. (Smaller value corresponds to better resolution.) (a) Unfiltered; (b) sharp-cutoff low-pass filtered. Low-pass filtering improves the specimen resolution for fine samplings under low-dose conditions. For single-layer graphene, the atomic resolution can be achieved at 1.4 Å, marked by the dashed lines in (a) and (b). The lowest dose to achieve this resolution is $5 \times 10^6 \, e^-/nm^2$ for an unfiltered image, and $2 \times 10^6 \, e^-/nm^2$ for a low-pass filtered image. The calculation is performed for the accelerating voltage of 80 kV.

Fig. 6. The specimen resolution approaches infinity for very low doses, at which the atom contrast is also close to 0 (Fig. 5). The specimen resolution improves as the dose increases and converges to 0.8 Å which is equal to the instrumental resolution at 80 kV on the SALVE II prototype.

Low-pass filtering effectively improves the specimen resolution for fine samplings under low dose conditions. For single-layer graphene, the atomic resolution can be achieved at 1.4 Å, marked by the dashed lines in Fig. 6a and b. The lowest dose to achieve this resolution is $5 \times 10^6 \, e^-/nm^2$ at the sampling of 0.15 Å/pixel or 0.075 Å/pixel for unfiltered images and $2 \times 10^6 \, e^-/nm^2$ at the samplings ≤ 0.075 Å/pixel for the low-pass filtered cases.

3.4. Determination of the optimum sampling

In order to obtain good object visibility at low doses, it is necessary to choose a suitable sampling. Coarse sampling causes both contrast and resolution loss and hyperfine sampling results in low contrast (Figs. 5 and 6).

Generally, it is enough to preserve the structure information up to the required specimen resolution d_s. The highest spatial frequency corresponding to the specimen resolution is $1/d_s$, which is smaller than or equal to the information limit defined by the instrument $1/d_i$. It should be at least guaranteed that the Nyquist frequency $q_N \geq 1/d_s$, so that the sampling δ satisfies $\delta = 1/(2q_N) \leq d_s/2$, based on the sampling theorem for discrete Fourier transform [41].

On the other hand, the damping of the MTF at the Nyquist frequency $q = q_N$ is so strong that the contrast corresponding to this frequency is only 10–15% compared with the case without any MTF damping (Fig. A1). Coarse sampling results in strong damping of the MTF, and accordingly weak atom contrast. This effect can be confirmed in the case of high electron dose ($> 5 \times 10^9 \, e^-/nm^2$), shown in Fig. B2, which is an extended version of Fig. 5a by exhibiting a broader range of electron dose. The maximum atom contrast decreases when the sampling gets coarse. At the sampling of 0.6 Å/pixel, the atom contrast obtained even with infinite electron dose is only about 1%.

The influence of the MTF damping on the image contrast can also be confirmed for low-pass filtered images (Fig. 5b). The filtered contrast for coarse sampling is lower than for fine sampling under the same dose condition.

For both unfiltered and filtered images, fine sampling (≤ 0.075 Å/pixel) is necessary in order to obtain high atom contrast. An ideal MTF profile (MTF ≈ 1) should cover the spatial frequency up to the required specimen resolution, indicating that $(1/d_s)/(2q_N) \leq 0.1$. Therefore the sampling should be

$$\delta = 1/(2q_N) \leq 0.1 d_s. \tag{16}$$

The maximum sampling also defines the lowest magnification ratio allowed:

$$M = \frac{\delta_p}{\delta} \geq 10\delta_p/d_s. \tag{17}$$

Here δ_p is the physical size of the detector pixel. If one wants to obtain an image with magnification ratio larger than $10\delta_p/d_s$, then the sampling δ should satisfy the relation $\delta \leq \delta_p/M$.

In order to obtain the maximum atom contrast for raw experimental images, the sampling should be finer than 0.075 Å/pixel and the required dose should be at least 5×10^9 e$^-$/nm^2 according to Fig. B2. However, such high electron dose is not realistic for beam-sensitive materials in TEM, which also means that it is barely possible to obtain an experimental image with the maximum atom contrast. For imaging with finite dose, the atom contrast obtained with fine sampling is not necessarily higher than obtained with coarse sampling even under the same dose conditions. An example is shown in Figs. 5 and B2, where for the electron doses between 5×10^6 e$^-$/nm^2 and 1×10^7 e$^-$/nm^2, the atom contrast at the sampling of 0.15 Å/pixel is higher than at finer samplings ≤ 0.075 Å/pixel.

In order to find out the best sampling under low-dose conditions, we substitute $C_d = C_W[SNR \cdot \sigma(I)]^2$ (Eq. (14)) and the approximation $SNR \approx \sqrt{N}$ (Eq. (9)) into the second term in Eq. (15). We obtain

$$\frac{(SNR)^2}{C_d^2 D} = \left[\frac{1}{C_W\sigma^2(I)}\right]^2 \frac{1}{\overline{N}D} = \left[\frac{1}{\delta C_W\sigma^2(I)}\right]^2 \frac{1}{D^2\overline{I}}. \tag{18}$$

We define

$$G(\delta) = \left[\frac{1}{\delta C_W\sigma^2(I)}\right]^2, \tag{19}$$

and since C_W as well as $\sigma(I)$ depends on the sampling δ, $G(\delta)$ is a function of δ only. In order to achieve the required specimen resolution d_s with low electron dose D, $G(\delta)$ must be small. If $G(\delta)$ has a minimum value, then the required dose D can also reach the minimum. In our case for graphene imaged with the SALVE II microscope, $G(\delta)$ is plotted with respect to the sampling δ in Fig. 7 for different accelerating voltages. Fig. 7 shows that $G(\delta)$ reaches the minimum for all accelerating voltages around 0.2 Å/pixel, indicating that the required electron dose to reach a specific resolution at this sampling is the lowest with the current experimental settings. The closest sampling in our examples is 0.15 Å/pixel. On the other hand, a fine specimen resolution under a given dose condition also indicates a large contrast value C_d (Eq. (15)). In the case of graphene, the distance between two neighbor atoms is 1.4 Å. As shown in Fig. 6a, the lowest electron dose to achieve this atomic resolution for graphene is 5×10^6 e$^-$/nm^2 at the sampling of 0.15 Å/pixel or 0.075 Å/pixel, and the maximum contrast of about 8.6% under this dose condition is obtained at the sampling of 0.15 Å/pixel, which is consistent with the analysis above.

As a summary, the optimum sampling and the lowest magnification ratio for raw image recorded with high dose are determined by the required specimen resolution d_s. The optimum sampling is determined by

$$\delta = \min\left[0.1 d_s, \frac{d_p}{M}\right] \quad (d_s \geq d_i, \ M \geq 10\delta_p/d_s). \tag{20}$$
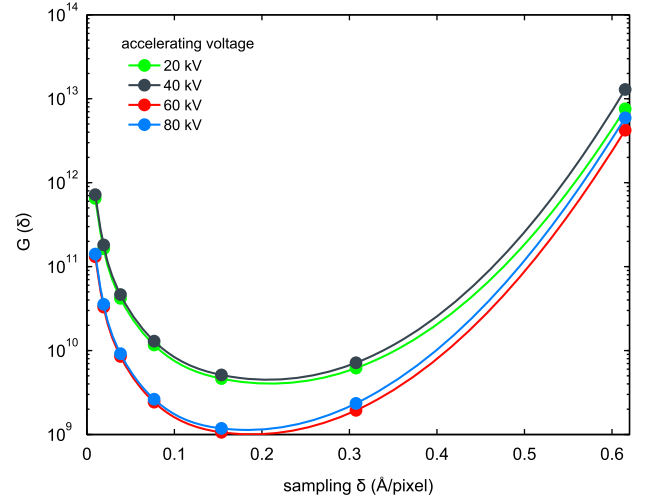

Fig. 7. The plot of $G(\delta) = 1/[\delta C_W \sigma^2(I)]^2$ with respect to the sampling δ for 20 kV, 40 kV, 60 kV and 80 kV on the current C_s/C_c-corrected SALVE II prototype. The usable aperture is 50 mrad, and parameters for calculations are listed in Table 1. At the sampling of 0.2 Å/pixel, G reaches the minimum, indicating that the electron dose D required to reach the resolution d_s also reaches the minimum.

For unknown samples, the required specimen resolution cannot be determined and one tends to record the image up to the information limit of the microscope. In this case the optimum sampling is determined by replacing d_s with d_i in Eq. (20).

For experimental images recorded with low dose, the optimum sampling is determined by the minimal value of Eq. (19). In order to improve the contrast of the low-dose images, low-pass filters can be applied. If one wants to maximize the atom contrast in the low-pass filtered images recorded with low dose, fine samplings ≤ 0.075 Å/pixel are required.

4. Summary

In this paper we have studied the influence of electron dose and sampling on the SNR, dose-dependent contrast and resolution using dose-dependent HRTEM image calculations. All three quantities improve with increasing electron dose, converging towards their values obtained at infinite dose. As sampling gets coarse, the SNR increases and the resolution deteriorates; the atom contrast improves as long as the damping of MTF is negligible. We have determined optimum sampling under high-dose and low-dose conditions. Under high-dose conditions, the optimum sampling depends mainly on the required specimen resolution. Under low-dose conditions, the best sampling is determined by our criteria that the required specimen resolution should be achieved with the minimal electron dose.

Appendix A. The fitting of MTFs for the SALVE II microscope

The MTF data (Fig. A1) for the SALVE microscope at 20 kV, 40 kV, 60 kV and 80 kV were previously measured using averaged single electron events detected by the T416 camera [38,39].

The measured MTFs (Fig. A1) are fitted by Eq. (A.1) and the coefficients a_1, a_2, a_3, a_4 as well as the coefficient of determination R^2 are listed in Table A1. The magnitude of R^2 shows the correlation between the original MTF profile and the fitted function. Large R^2 value indicates good fitting.

$$MTF(q) = \frac{a_1 - a_2}{1 + \left(\frac{q}{2a_3 q_N}\right)^{a_4}} + a_2 \tag{A.1}$$

Here q_N is the Nyquist frequency related to the sampling δ by $\delta = 1/(2q_N)$.

Usually the x-axis of the MTF profile represents the frequency corresponding to a certain feature sampled with n pixels in real space, and $1/n$ has the unit of pixel^{-1}. Here we have used another notation in order to facilitate the image calculation. By multiplying both the numerator and the denominator with the sampling δ, we obtain

$$\frac{1}{n} = \frac{\delta}{n\delta} = \frac{1/n\delta}{1/\delta}. \tag{A.2}$$

The denominator is the reciprocal of the sampling δ, which equals two times of the Nyquist frequency q_N. The numerator represents the spatial frequency q corresponding to the feature sampled with n pixels in real space. We obtain

$$\frac{1}{n} = q\delta = \frac{q}{2q_N} \tag{A.3}$$
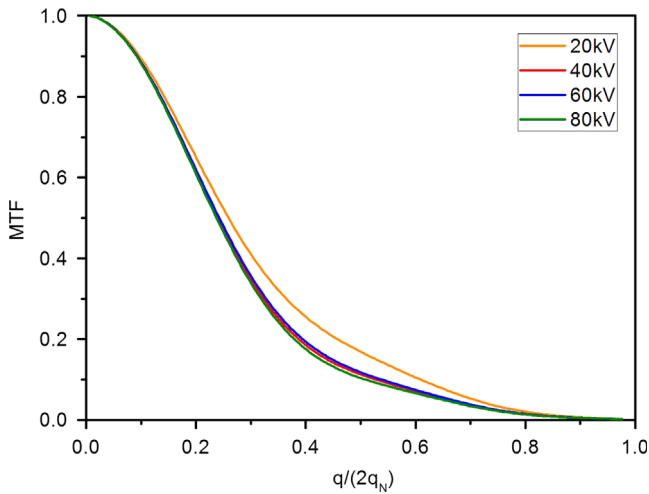
Fig. A1. Experimentally measured MTFs for the SALVE II microscope at 20 kV, 40 kV, 60 kV and 80 kV. At Nyquist frequency where $q/(2q_N) = 0.5$, the MTF is between 0.1 and 0.15, indicating that the image contrast corresponding to this frequency has a loss of 85–90%.

Table A1
The fitting coefficients of a_1, a_2, a_3 and a_4 for Eq. (A.1).

HT (kV)	a_1	a_2	a_3	a_4	R^2
20	99.97	−6.71	0.27	2.19	0.99972
40	98.75	−2.87	0.24	2.55	0.99971
60	98.83	−3.14	0.25	2.53	0.99973
80	98.48	−2.52	0.24	2.63	0.99965

Appendix B. Determination of the factor γ in Eq. (14)

We calculated the coefficient of determination R^2 showing the correlation between the images calculated with finite electron doses and the ones calculated with infinite electron dose (Fig. B1). If we define

$$S_{12} = \sum_{j=1}^{J} [Pois(D\delta^2 I_j) - \overline{Pois(D\delta^2 I_j)}][I_j - \overline{I}], \tag{B.1}$$

$$S_{11} = \sum_{j=1}^{J} [Pois(D\delta^2 I_j) - \overline{Pois(D\delta^2 I_j)}]^2, \tag{B.2}$$

$$S_{22} = \sum_{j=1}^{J} [I_j - \overline{I}]^2. \tag{B.3}$$

Then the coefficient of determination is

$$R^2 = \frac{S_{12}^2}{S_{11} S_{22}} \tag{B.4}$$

The coefficient R^2 lies in the range of $[0, 1]$, where the number 1 indicates a perfect match and 0 indicates no match at all. R^2 increases smoothly with respect to the electron dose. When $R^2 = 1$, the atom contrast equals the value obtained with infinite dose $C_d = (I_b - I_a)/I_b$; and when $R^2 = 0$, the atom contrast is $C_d = 0$. Therefore we can define the dose-dependent contrast by scaling R^2 with the Weber contrast $C_W = (I_b - I_a)/I_b$, resulting in Fig. B2. One can see that for coarse sampling, the maximum atom contrast is smaller than for fine sampling. This trend is consistent with the evolution of atom contrast with respect to the electron dose (Fig. 1), and we can use Eq. (14) to fit the curves in Fig. B2 in the following way:

$$R^2 \left| \frac{I_b - I_a}{I_b} \right| = \left(\frac{\sigma(N)}{\overline{N}\sigma(I)}\right)^{-\gamma} \left| \frac{I_b - I_a}{I_b} \right| \tag{B.5}$$

results in

$$\ln\frac{1}{R^2} = \gamma \ln\frac{\sigma(N)}{\overline{N}\sigma(I)}. \tag{B.6}$$

Here all the terms in the logarithms are larger than 0. By linear fitting of $\ln[\sigma(N)/(\overline{N}\sigma(I))]$ and $\ln(1/R^2)$, we can obtain the coefficient γ which is the slope of the line. The fitting is displayed in Fig. B3, where all the lines show similar slope.

The corresponding γ values for different samplings obtained through linear fitting in Fig. B3 is listed in Table B1. Since the
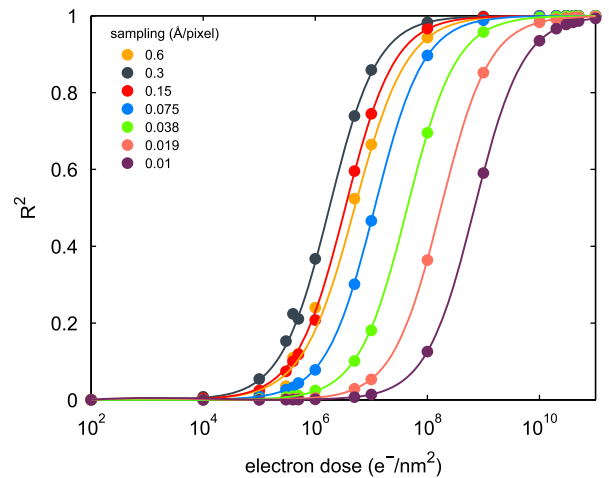

Fig. B1. The coefficient of determination R^2 shows the correlation between the images calculated with finite and infinite electron doses at different samplings. The calculation is performed for the accelerating voltage of 80 kV.
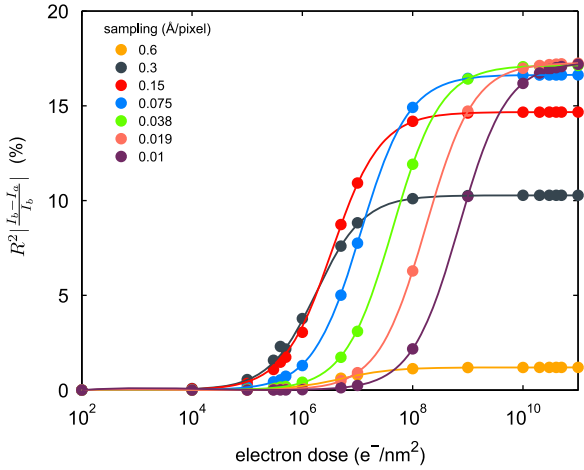
Fig. B2. The atom contrast obtained by scaling the coefficient R^2 with the contrast achieved under infinite dose, namely $R^2|(I_b - I_a)/I_b|$. At coarse samplings, the maximum atom contrast is lower than at fine samplings. The calculation is performed for the accelerating voltage of 80 kV.
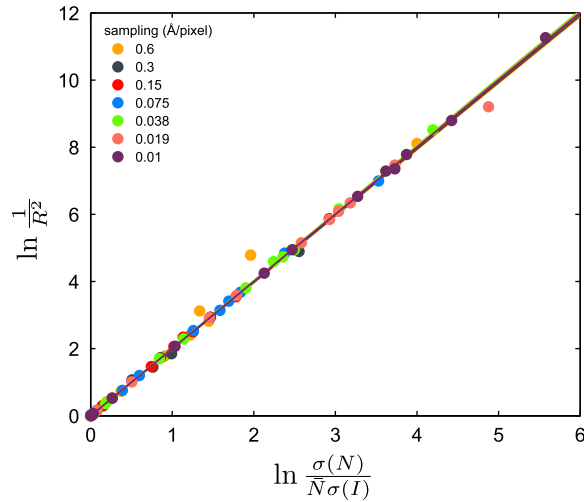
Fig. B3. The linear fitting of $\ln[\sigma(N)/(\overline{N}\sigma(I))]$ and $\ln\left(1/R^2\right)$. The slope of the line is the coefficient γ and the slope is very close for different samplings. The calculation is performed for the accelerating voltage of 80 kV.

Table B1
The γ values fitted for different samplings based on Eq. (B.6).

Sampling (Å/pixel)	γ
0.6	1.981
0.3	1.987
0.15	1.998
0.075	2.003
0.038	2.013
0.019	2.006
0.01	2.000

results are very close, we can take $\gamma = 2$ for all samplings. This result $\gamma = 2$ for all samplings is not surprising. In the case of high dose, $Pois(D\delta^2 I_j) \approx D\delta^2 I_j$ and $\overline{Pois(D\delta^2 I_j)} \approx D\delta^2 \overline{I}$. Therefore

$$S_{12} = \sum_{j=1}^{J}\left[Pois(D\delta^2 I_j) - \overline{Pois(D\delta^2 I_j)}\right][I_j - \overline{I}]$$

$$\approx D\delta^2 \sum_{j=1}^{J}[I_j - \overline{I}]^2 = D\delta^2 S_{22}, \qquad (B.7)$$

$$R^2 = \frac{S_{12}^2}{S_{11}S_{22}} \approx \frac{(D\delta^2)^2 \sum_{j=1}^{J}[I_j - \overline{I}]^2}{\sum_{j=1}^{J}[Pois(D\delta^2 I_j) - \overline{Pois(D\delta^2 I_j)}]^2}$$

$$= \left[\frac{D\delta^2 \sigma(I)}{\sigma(N)}\right]^2 \approx \left[\frac{D\delta^2 \overline{I}\sigma(I)}{\sigma(N)}\right]^2 = \left[\frac{\overline{N}\sigma(I)}{\sigma(N)}\right]^2. \qquad (B.8)$$

The relation between R and $\overline{N}\sigma(I)/\sigma(N)$ is then clarified. Here the relation $\overline{I} \approx 1$ has been used.

References

[1] H. Rose, Outline of a spherically corrected semi-aplanatic medium-voltage TEM, Optik 85 (1990) 19–24.

[2] M. Haider, S. Uhlemann, E. Schwan, H. Rose, B. Kabius, K. Urban, Electron microscopy image enhanced, Nature 392 (1998) 768–769.

[3] O. Krivanek, N. Dellby, A. Lupini, Towards sub-Å electron beams, Ultramicroscopy 78 (1) (1999) 1–11.

[4] C. Jia, M. Lentzen, K. Urban, Atomic-resolution imaging of oxygen in perovskite ceramics, Science 299 (5608) (2003) 870–873.

[5] P.D. Nellist, M.F. Chisholm, N. Dellby, O. Krivanek, M. Murfitt, Z. Szilagyi, A.R. Lupini, A. Borisevich, W. Sides, S.J. Pennycook, Direct sub-angstrom imaging of a crystal lattice, Science 305 (5691) (2004) 1741.

[6] Y. Sato, K. Suenaga, S. Okubo, T. Okazaki, S. Iijima, Structures of D 5 d-C80 and I h-Er3n@ C80 fullerenes and their rotation inside carbon nanotubes demonstrated by aberration-corrected electron microscopy, Nano Lett. 7 (12) (2007) 3704–3708.

[7] O.L. Krivanek, M.F. Chisholm, V. Nicolosi, T.J. Pennycook, G.J. Corbin, N. Dellby, M.F. Murfitt, C.S. Own, Z.S. Szilagyi, M.P. Oxley, et al., Atom-by-atom structural and chemical analysis by annular dark-field electron microscopy, Nature 464 (7288) (2010) 571–574.

[8] U. Kaiser, J. Biskupek, J.C. Meyer, J. Leschner, L. Lechner, H. Rose, M. Stöger-Pollach, A.N. Khlobystov, P. Hartel, H. Müller, M. Haider, S. Eyhusen, G. Benner, Transmission electron microscopy at 20 kV for imaging and spectroscopy, Ultramicroscopy 111 (2011) 1239–1246.

[9] T. Zoberbier, T.W. Chamberlain, J. Biskupek, N. Kuganathan, S. Eyhusen, E. Bichoutskaia, U. Kaiser, A.N. Khlobystov, Interactions and reactions of transition metal clusters with the interior of single-walled carbon nanotubes imaged at the atomic scale, J. Am. Chem. Soc. 134 (6) (2012) 3073–3079.

[10] H. Sawada, T. Sasaki, F. Hosokawa, S. Yuasa, M. Terao, M. Kawazoe, T. Nakamichi, T. Kaneyama, Y. Kondo, K. Kimoto, K. Suenaga, Higher-order aberration corrector for an image-forming system in a transmission electron microscope, Ultramicroscopy 110 (2010) 958–961.

[11] O.L. Krivanek, N. Dellby, M.F. Murfitt, M.F. Chisholm, T.J. Pennycook, K. Suenaga, V. Nicolosi, Gentle STEM: ADF imaging and EELS at low primary energies, Ultramicroscopy 110 (8) (2010) 935–945.

[12] M. Haider, P. Hartel, H. Müller, S. Uhlemann, J. Zach, Information transfer in a TEM corrected for spherical and chromatic aberration, Microsc. Microanal. 16 (04) (2010) 393–408.

[13] H. Rose, Prospects for aberration-free electron microscopy, Ultramicroscopy 103 (1) (2005) 1–6.

[14] R.M. Glaeser, K.A. Taylor, Radiation damage relative to transmission electron microscopy of biological specimens at low temperature: a review, J. Microsc. 112 (1) (1978) 127–138.

[15] H. Rose, Future trends in aberration-corrected electron microscopy, Philos. Trans. R. Soc. A: Math. Phys. Eng. Sci. 367 (1903) (2009) 3809–3823.

[16] R. Egerton, Control of radiation damage in the TEM, Ultramicroscopy 127 (0) (2013) 100–108.

[17] R. Egerton, Mechanisms of radiation damage in beam-sensitive specimens, for TEM accelerating voltages between 10 and 300 kV, Microsc. Res. Tech. 75 (11) (2012) 1550–1556.

[18] Y. Chen, W. Sibley, Study of ionization-induced radiation damage in MgO, Phys. Rev. 154 (3) (1967) 842.

[19] L. Reimer, H. Kohl, Transmission Electron Microscopy: Physics of Imaging Formation, vol. 36, Springer, New York, 2008.

[20] G. Algara-Siller, S. Kurasch, M. Sedighi, O. Lehtinen, U. Kaiser, The pristine atomic structure of MoS_2 monolayer protected from electron radiation damage by graphene, Appl. Phys. Lett. 103 (2013) 203107.

[21] J. Biskupek, P. Hartel, M. Haider, U. Kaiser, Effects of residual aberrations explored on single-walled carbon nanotubes, Ultramicroscopy 116 (2012) 1–7.

[22] J. Barthel, A. Thust, On the optical stability of high-resolution transmission electron microscopes, Ultramicroscopy 134 (2013) 6–17.

[23] S. Schramm, S. van der Molen, R. Tromp, Intrinsic instability of aberration-corrected electron microscopes, Phys. Rev. Lett. 109 (16) (2012) 163901.

[24] S. Uhlemann, H. Müller, P. Hartel, J. Zach, M. Haider, Thermal magnetic field noise limits resolution in transmission electron microscopy, Phys. Rev. Lett. 111 (July) (2013) 046101.

[25] M. Barth, R. Bryan, R. Hegerl, Approximation of missing-cone data in 3D electron microscopy, Ultramicroscopy 31 (4) (1989) 365–378.

[26] R.M. Glaeser, K.H. Downing, Assessment of resolution in biological electron crystallography, Ultramicroscopy 47 (1) (1992) 256–265.

[27] C. Sorzano, L. De La Fraga, R. Clackdoyle, J. Carazo, Normalizing projection images: a study of image normalizing procedures for single particle three-dimensional electron microscopy, Ultramicroscopy 101 (2) (2004) 129–138.

[28] M. van Heel, M. Schatz, Fourier shell correlation threshold criteria, J. Struct. Biol. 151 (3) (2005) 250–262.

[29] F. Förster, S. Pruggnaller, A. Seybert, A.S. Frangakis, Classification of cryo-electron sub-tomograms using constrained correlation, J. Struct. Biol. 161 (3) (2008) 276–286.

[30] M. Malac, M. Beleggia, R. Egerton, Y. Zhu, Imaging of radiation-sensitive samples in transmission electron microscopes equipped with zernike phase plates, Ultramicroscopy 108 (2) (2008) 126–140.

[31] Z. Lee, J.C. Meyer, H. Rose, U. Kaiser, Optimum HRTEM image contrast at 20 kV and 80 kV exemplified by graphene, Ultramicroscopy 112 (2012) 39–46.

[32] Z. Lee, H. Rose, R. Hambach, P. Wachsmuth, U. Kaiser, The influence of inelastic scattering on EFTEM images-exemplified at 20 kV for graphene and silicon, Ultramicroscopy 134 (2013) 102–112.

[33] K.-H. Herrmann, D. Krahl, The detection quantum efficiency of electronic image recording systems, J. Microsc. 127 (1) (1982) 17–28.

[34] W. De Ruijter, J. Weiss, Methods to measure properties of slow-scan CCD cameras for electron detection, Rev. Sci. Instrum. 63 (10) (1992) 4314–4321.

[35] M. Vulovic, B. Rieger, L. Van Vliet, A. Koster, R. Ravelli, A toolkit for the characterization of CCD cameras for transmission electron microscopy, Acta Crystallogr. Sect. D: Biol. Crystallogr. 66 (1) (2009) 97–109.

[36] M. De Graef, Introduction to Conventional Transmission Electron Microscopy, Cambridge University Press, Cambridge, 2003.

[37] H. Rose, Corrector, Jan. 17 1992, Offenlegungsschrift DE 42 04 512 A 1.

[38] R. Ghadimi, I. Daberkow, C. Kofler, P. Sparlinek, H. Tietz, Characterization of 16 megapixel CMOS detector for TEM by evaluating single events of primary electrons, Microsc. Microanal. 17 (S2) (2011) 1208–1209.

[39] H. Tietz, R. Ghadimi, I. Daberkow, Single electron events in TEM—measuring the resolution of fiber optic coupled CMOS cameras, Imag. Microsc. 14 (2012) 46–48.

[40] A.A. Michelson, Studies in Optics, Courier Dover Publications, New York, 1995.

[41] R.N. Bracewell, R. Bracewell, The Fourier Transform and its Applications, 31999, McGraw-Hill, New York, 1986.